
SCALING TRANSFORMATION OF THE MULTIMODE NONLINEAR SCHRÖDINGER EQUATION FOR PHYSICS-INFORMED NEURAL NETWORKS

A PREPRINT

 Ivan Chuprov¹,  Dmitry Efremenko²,  Jiexing Gao¹,  Pavel Anisimov¹,  Viacheslav Zemlyakov¹

September 30, 2022

¹ Huawei Technologies Co., Ltd, Central Research Institute, Shenzhen, China

² Remote Sensing Technology Institute (IMF), German Aerospace Center (DLR), Oberpfaffenhofen, Germany

ABSTRACT

Single-mode optical fibers (SMFs) have become the backbone of modern communication systems. However, their throughput is expected to reach its theoretical limit in the nearest future. Utilization of multimode fibers (MMFs) is considered as one of the most promising solutions rectifying this capacity crunch. Nevertheless, differential equations describing light propagation in MMFs are a way more sophisticated than those for SMFs, which makes numerical modelling of MMF-based systems computationally demanding and impractical for the most part of realistic scenarios. Physics-informed neural networks (PINNs) are known to outperform conventional numerical approaches in various domains and have been successfully applied to the nonlinear Schrödinger equation (NLSE) describing light propagation in SMFs. A comprehensive study on application of PINN to the multimode NLSE (MMNLSE) is still lacking though. To the best of our knowledge, this paper is the first to deploy the paradigm of PINN for MMNLSE and to demonstrate that a straightforward implementation of PINNs by analogy with NLSE does not work out. We pinpoint all issues hindering PINN convergence and introduce a novel scaling transformation for the zero-order dispersion coefficient that makes PINN capture all relevant physical effects. Our simulations reveal good agreement with the split-step Fourier (SSF) method and extend numerically attainable propagation lengths up to several hundred meters. All major limitations are also highlighted.

Keywords Physics-informed neural networks · Nonlinear Schrödinger equation · Split-step Fourier method

1 Introduction

Fiber-optic communication systems employ optical fibers for information transfer. The state-of-the-art fiber-optic communication systems have advanced dramatically in the last two decades. The so called bit rate-distance product BL , where B and L stand for the bit rate and the repeater spacing, respectively, has increased by three orders of magnitude in the last decade [1, 2]. However, ever-growing information traffic demands enforced reconsideration of future optical communication technology and boosted research on novel transmission approaches, such as mode division multiplexing (MDM) [3]. Opposed to current single-mode fibers (SMFs) systems, MDM implies utilization of multimode fibers (MMFs) that support simultaneous propagation of multiple guided modes. These modes, in turn, can be encoded as independent signals and thus enable spatial multiplexing. Despite such systems have already surpassed the important milestone of 1 Pb/s data throughput [4], MDM is still in its infancy. It is largely because of additional descriptive complexity of light propagation in MMFs that is mostly associated with intertwining of different modes. Namely, conventional single-mode nonlinear Schrödinger equation (NLSE) is replaced by a system of

coupled differential equations, referred to as multimode NLSE (MMNLSE). Ubiquitous tools for solving NLSE, such as the split-step Fourier method (SSF) [5, 6], are naturally extendable to the case of MMNLSE but require tremendous computational effort, whereas realistic MMF systems of 200-500 m [7] cannot be decently modeled without sacrificing MMNLSE generality. This fact gives rise to new challenges that numerical algorithms have to address. Such algorithms are required to model accurately the signal propagation in fibers and, for example, to design techniques for compensating signal distortions [8].

Recently, machine learning (ML) techniques were applied to NLSE [9]. One of the most promising ML tools for solving NLSE is physics-informed neural networks (PINNs). PINNs belong to universal function approximators that are trained with an eye on the underlying physical laws rather than given on datasets [10]. In practice, PINNs are used to solve partial differential equations (PDEs) and in this regard, are often considered as a mesh-free alternative to traditional numerical solvers. The idea of the PINN approach consists in training a neural network so that it satisfies both a given PDE and boundary/initial conditions. Consequently, the loss function to be minimized during the training process consists of the residual w.r.t. the PDE (i.e. when substituting the PINN into the original PDE) and the residual w.r.t. the initial conditions. The key feature of the PINNs approach is that the corresponding partial derivatives of the neural network are computed with help of automatic differentiation tools implemented in ML libraries (e.g. PyTorch). In this manner, the loss function can be minimized and the given PDE can be solved using the tools of ML in a weak formulation. It can be shown that PINNs methodology is similar to Newton-Krylov solvers [11, 12] and the finite element method [13]. In addition, PINNs are conceptually similar to the Ritz method [14].

PINNs were applied to a single-mode NLSE and validated against the SSF [15–18]. Although PINNs can provide accurate results, their current training time is larger than that of SSF. Therefore, PINNs cannot compete with the classical solvers. However, some features of PINNs motivate their further development resulting in a large amount of modifications (see [19–22] and references therein). The first advantage of PINNs is their universality, as they have been applied to problems in the wide range of fields [23–25]. Secondly, PINNs have the potential to be an effective analysis tool for long-distance and high-channel loading scenarios, as its complexity raises slower with the pulse energy than that of SSF [17]. Thirdly, the training time of PINNs can be significantly reduced via transfer-learning. It has been estimated that the total number of peer-reviewed papers about PINNs applications has exceeded 2000, and this quantity has grown from 30 papers in 2018 to 1300 in 2021 [26].

The main drawback of PINNs (apart from the current long training time) is that they may fail to converge in some cases depending on the parameters entering a PDE. It was noted that the convergence of PINN for solving NLSE is much slower than that for the linear Schrödinger equation, i.e. more time is required to capture nonlinear dependencies [16]. Nevertheless, such an observation does not explain why in some cases PINNs yield no solution at all. An attempt to study these PINNs issues from the mathematical point of view was done in [27]. Besides, PINNs were improved by adding new modifications in the neural network [22, 27, 28]. However, these approaches are not suitable for MMNLSE, since the PINNs fail to converge, and to the best of our knowledge, no such results have been reported so far.

In this paper, we propose a recipe for solving MMNLSE with PINN. Considering this problem from the physical point of view, we use a scale transformation of MMNLSE parameters, which allows leveling a large difference between coefficients and leads to a successful solution for a hundred of meters. We also note that it is necessary to consider the maximum of fiber length for PINN only with a energy value. We demonstrate that the energy value affects the nonlinear length which constrains PINNs.

This paper is organized as follows. In Section 2, we introduce a suitable PINN configuration. In Section 3, NLSE is reviewed and the origin of numerical problems for PINNs is discussed. A frame transformation and normalization procedure are analyzed and the scaling transformation is proposed which allows us to bring MMNLSE to the PINN solvable form. Section 4 contains results of numerical experiments and provide comparison of the PINN with SSF. The paper is concluded with a summary.

2 PINN configuration

We developed a PINN framework using the PyTorch library [29] as a backend. The neural network configuration is organized as follows. The PINN model consists of 6 ResNet blocks with 150 neurons and Tanhshrink activation functions in each of them. This configuration is chosen empirically: other numbers of blocks, neurons, or changes in other parameters worsened our results. In our simulations we also observed that Tanhshrink performs better than ReLU and Tanh activation functions. The actual value of the learning rate is governed by the scheduler. It multiplies the current value of the learning rate by factor (0.9 by default) if the loss function is not reduced after a certain amount of iterations (30 iterations by default). The minimal learning rate value is set to $1e-7$. The partial derivatives are computed by using built-in features of PyTorch automatic differentiation. The PINN takes the pairs of T and z as

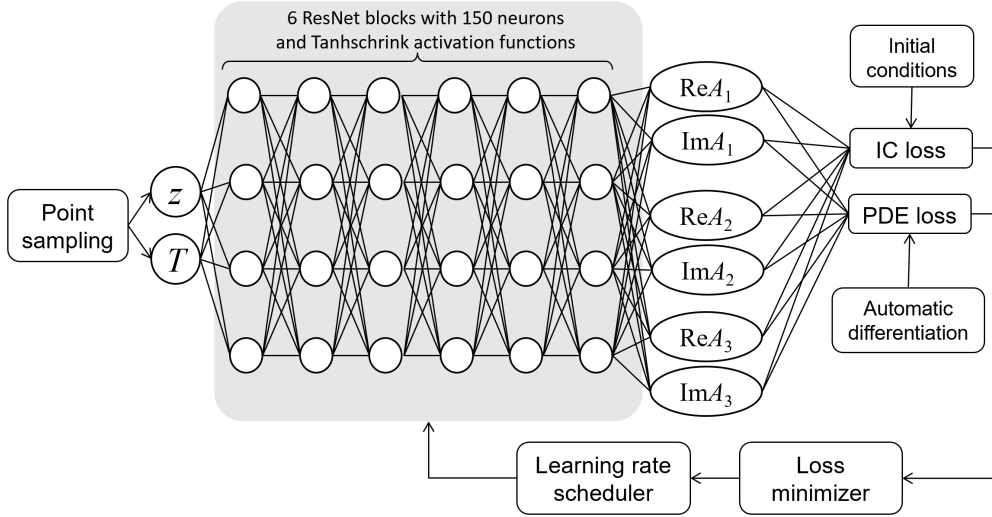


Figure 1: PINN configuration used in this study

input and returns real and imaginary components for each mode. Thus, PINN has 2 inputs and 6 outputs. The PINN structure is summarized in Fig. 1. The training is run on GPU NVidia Tesla V100 16GB.

240000 sample points are mainly used. We have found that this is sufficient to obtain satisfactory results in our cases. Empirically it was found that by taking more sampling points around $T = 0$ (i.e. where the function changes faster), PINN accuracy can be improved. Keeping that in mind, we adopt a heterogeneous algorithm for random point sampling which provides 90% of points in the time domain corridor $[-T_{\max}/2, T_{\max}/2]$. The weights of the network are initialized by using the Xavier method [30].

Note that the loss function is not a straightforward measure of the PINN accuracy. Therefore, for validation purposes, the PINN results are compared with the SSF solution. Optionally, frame transformation (2)-(3), pulse normalization (5) as well as the novel scaling transformation (28)-(29) for $\delta\beta_0^{(p)}$ can be enabled.

3 Theory

3.1 Problem background

Optical fibers consist of a core surrounded by a cladding. The former has higher values of the refractive index that results in total internal reflection, and thus confines light (Fig. 2(a)). Light propagation through an MMF is derived from the Maxwell's equation, which is solved by separation of variables. The transversal part satisfies the Helmholtz equation that in the case of large core diameters enables multiple solutions, referred to as modes. The fiber, in this case, is called an MMF. Modal content of such optical fibers strongly depends on the shape of the refractive index profile function (Fig. 2(b)) that describes its evolution along the radial direction. If $n_{\text{core}} \simeq n_{\text{clad}}$, the so-called weakly-guided approximation takes place and we call the resulting solution the linearly-polarized modes (LP). These are classified by two indices originating from the Helmholtz equation and are ordered in the descending order with respect to their propagation constants determining phase velocities of the modes [2]. If the shape of the refractive index profile function fulfills a quasi-parabolic law (the so-called graded-index profile function or GRIN, Fig. 2(b)), modes become degenerate with respect to the propagation constants and reveal similar propagation behaviour.

In this work, we consider propagation of the first three LP modes implying that degenerate partners are omitted, i.e. LP_{01} , LP_{11a} and LP_{21a} (Fig. 2(c)). In what follows, we directly address them by their appearance order as 1,2 and 3.

3.2 MMNLSE and the frame transformation

Evolution of a laser pulse in MMF is described by MMNLSE [2]

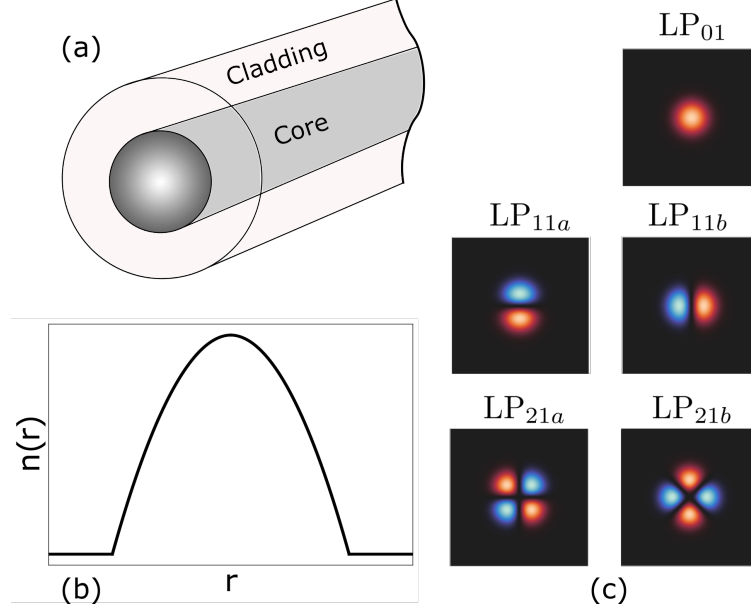


Figure 2: Modes in multimode fiber. (a) Schematic of a graded-index multimode fiber; (b) GRIN profile; (c) Intensity profiles of first 5 modes.

$$\begin{aligned} \mathfrak{N}(A_p) \equiv & -\frac{\partial A_p}{\partial z} + i\delta\beta_0^{(p)} A_p - i\delta\beta_1^{(p)} \frac{\partial A_p}{\partial T} - i\frac{\beta_2^{(p)}}{2} \frac{\partial^2 A_p}{\partial T^2} \\ & + i\gamma_S |A_p|^2 A_p + i \sum_{n \neq p} \gamma_C^{(n)} |A_n|^2 A_p = 0, \end{aligned} \quad (1)$$

where $A(z, T)$ is the electric field temporal envelope, z is the propagation distance, $\delta\beta_j^{(p)} = \beta_j^{(p)} - \text{Re}\beta_j^{(0)}$, $\beta_j^{(p)}$ is the j th order dispersion coefficient for the p th mode, T is the time under time-retarded frame, while γ_S and $\gamma_C^{(n)}$ are the nonlinear coefficients, namely self-phase and cross-phase modulations Kerr coefficients, respectively [2]. Nonlinearity is mainly responsible for coupling between modes and leads to various unexpected effects and problems. In this paper, four wave mixing, Raman scattering and the fiber losses are neglected.

During the learning process, PINN is substituted into Eq. (1) as A_p and partial derivatives are computed by automatic differentiation tools. The PDE residual is then equal to $\mathfrak{N}(\text{PINN})$ which is to be minimized together with the initial condition residual. Note if the coefficients in Eq. (1) differ by several orders of magnitude, the PINN becomes less sensible to the terms with small ones, and, therefore, their influence cannot be captured.

It is a common practice to consider A as a function of unitless variables ζ and t defined through the following relations [31]

$$z = k_1 L_D \zeta, \quad T = k_2 T_0 t, \quad (2)$$

where

$$k_1 = \frac{L_{\max}}{L_D}, \quad k_2 = \frac{T_{\max}}{T_0}, \quad (3)$$

L_D is the dispersion length given by

$$L_D = \frac{T_0^2}{|\beta_2|}, \quad (4)$$

with $[-T_{\max}/2, T_{\max}/2]$ being the time window and T_0 the initial width of the pulse. Eqs. (2)-(3) are referred to as frame transformation. In addition, A can be normalized by the peak power of the pulse P_0 ,

Table 1: Coefficients of Eq. (1)

λ , nm	Terms					
	$\partial A_p/\partial z$	A_p	$\partial A_p/\partial t$	$\partial^2 A_p/\partial t^2$	$ A_p ^2 A_p$	$ A_n ^2 A_p$
	Coefficients					
	1	$\delta\beta_0^{(p)}$, m ⁻¹	$\delta\beta_1^{(p)}$, ps/m	$\beta_2^{(p)}/2$, ps ² /m	γ_S , W ⁻¹ /m	$\gamma_C^{(n)}$, W ⁻¹ /m*
1030	1	-11328	0.0079	0.0096	0.0011	0.0006

* Specified maximum coefficient values for all modes

Table 2: Coefficients of Eq. (6) for different values of pulse energy E and fiber length L

E , nJ	P_0 , W	L , m	L_D , m	L_{NL} , m	Terms					
					$\partial U_p/\partial \zeta$	U_p	$\partial U_p/\partial t$	$\partial^2 U_p/\partial t^2$	$ U_p ^2 U_p$	$ U_n ^2 U_p$
					Coefficients					
					1	$k_1\delta\beta_0^{(p)}$	$k_1\delta\beta_1^{(p)}/k_2$	k_1c/k_2^2	k_1d	$k_1d(\gamma_C^{(n)}/\gamma_S)^*$
10	9393	5	18.8	0.09	1	-3009	1.3e-5	-4.8e-6	53.85	107.7
0.1	93	100	18.8	9.28	1	-60182	2.5e-4	-9.6e-5	10.77	21.54
1e-3	0.93	1000	18.8	928	1	-601829	8.4e-4	-1e-4	1.077	2.154
1e-6	9.3e-3	1000	18.8	928475	1	-601829	8.4e-4	-1e-4	1e-3	2.1e-3

* Specified maximum coefficient values for all modes

$$A = \sqrt{P_0}U. \quad (5)$$

Applying transformations (2)-(3) and (5) to Eq. (1), we obtain the MMNLSE for the normalized quantity U in the transformed frame (ξ, t)

$$i\frac{\partial U_p}{\partial \zeta} + k_1\delta\beta_0^{(p)}U_p + \frac{k_1\delta\beta_1^{(p)}}{k_2}\frac{\partial U_p}{\partial t} + \frac{k_1c}{k_2^2}\frac{\partial^2 U_p}{\partial t^2} + k_1d|U_p|^2U_p + k_1d\sum_{n \neq p}\frac{\gamma_C^{(n)}}{\gamma_S}|U_n|^2U_p = 0, \quad (6)$$

where

$$c = \frac{-\text{sign}(\beta_2)}{2}, \quad d = \frac{L_D}{L_{NL}}, \quad (7)$$

while

$$L_{NL} = \frac{1}{\gamma P_0} \quad (8)$$

is the so-called nonlinear length. Coefficients used in this study are given in Tables 1, 2 for Eq. (1) and (6) respectively. Examples of coefficients for cases considered in this study are shown in Table for Eq. and Table for Eq. (1). Note, the coefficients in Eq. (1) depend on the fiber material and the pulse wavelength, while the weights at the terms of Eq. (6) additionally depend on the pulse energy and the time window. It can be seen that transformations (2)-(3) and (5) change the order of certain coefficients, which appear to be beneficial for some cases (e.g. energies $\sim 1^{-6}$ nJ). However, these transformations do not solve the problem associated with large values of $\delta\beta_0^{(p)}$ (as compared to other coefficients in Eq. (6)), but rather increase the difference between them. From the physical point of view, high values of $\delta\beta_0^{(p)}$ cause the high-frequency dependency of U_p with respect to z , thus creating a problem for PINNs. Our goal is to reduce the large values of the $\delta\beta_0^{(p)}$ coefficients in a reasonable way. We consider the Schrödinger equation step by step, adding to it multimodality and nonlinearity.

3.3 Single-mode linear case

We start with a single-mode linear equation and revise the derivation of its solution. The linear single mode equation for $A(z, T)$ reads as follows:

$$i \frac{\partial A}{\partial z} = \frac{\beta_2}{2} \frac{\partial^2 A}{\partial T^2}. \quad (9)$$

The initial condition is given by the Gaussian pulse

$$A(0, T) = \exp \left\{ -\frac{T^2}{2T_0^2} \right\}, \quad (10)$$

where T_0 is the half-width, that related to the full-width at half-maximum (FWHM) of the pulse as

$$T_{FWHM} = 2(\ln 2)^{1/2} T_0 \approx 1.665 T_0. \quad (11)$$

Following [2], we can analytically solve Eq. (9) (for details see Appendix 1). The final result reads as

$$A(z, T) = \frac{T_0}{\sqrt{T_0^2 - i\beta_2 z}} \exp \left[-\frac{T^2}{2(T_0^2 - i\beta_2 z)} \right]. \quad (12)$$

3.4 Multimode linear case

Now we consider the linear equation with the additional term $\delta\beta_0^{(p)} A$ which is present in the multimode equation

$$i \frac{\partial A}{\partial z} = \frac{\beta_2}{2} \frac{\partial^2 A}{\partial T^2} + \delta\beta_0^{(p)} A. \quad (13)$$

Applying Fourier transform we obtain

$$i \frac{\partial \hat{A}}{\partial z} = -\frac{1}{2} \beta_2 \omega^2 \hat{A} + \delta\beta_0^{(p)} \hat{A} \quad (14)$$

$$= \left(-\frac{1}{2} \beta_2 \omega^2 + \delta\beta_0^{(p)} \right) \hat{A}. \quad (15)$$

Solution of Eq (15) reads as follows

$$\hat{A}(z, \omega) = \hat{A}(0, \omega) \exp \left\{ \left(\frac{i}{2} \beta_2 \omega^2 - i\delta\beta_0^{(p)} \right) z \right\}. \quad (16)$$

The inverse Fourier transform yields

$$A(z, T) = \frac{1}{2\pi} \int_{-\infty}^{+\infty} \hat{A}(0, \omega) \times \exp \left\{ \left(\frac{i}{2} \beta_2 \omega^2 - i\delta\beta_0^{(p)} \right) z - i\omega T \right\} d\omega. \quad (17)$$

Using the initial condition (10), we obtain

$$A(z, T) = \frac{1}{2\pi} \int_{-\infty}^{+\infty} T_0 \exp \left\{ -\frac{1}{2} T_0^2 \omega^2 \right\} \times \exp \left\{ \left(\frac{i}{2} \beta_2 \omega^2 - i\delta\beta_0^{(p)} \right) z - i\omega T \right\} d\omega. \quad (18)$$

The term $\exp \left\{ -i\delta\beta_0^{(p)} z \right\}$ can be moved outside the integral

$$A(z, T) = \exp \left\{ -i\delta\beta_0^{(p)} z \right\} \frac{1}{2\pi} \int_{-\infty}^{+\infty} T_0 \exp \left\{ -\frac{1}{2} T_0^2 \omega^2 \right\} \times \exp \left\{ \frac{i}{2} \beta_2 \omega^2 z - i\omega T \right\} d\omega. \quad (19)$$

The final result reads as follows

$$A(z, T) = \exp \left\{ -i\delta\beta_0^{(p)} z \right\} \frac{T_0}{\sqrt{T_0^2 - i\beta_2 z}} \times \exp \left\{ -\frac{T^2}{2(T_0^2 - i\beta_2 z)} \right\}. \quad (20)$$

Recalling that A is a function of $A(z, T, \delta\beta_0^{(p)})$, with help of Eqs. (12) and (20) we obtain

$$A(z, T, \delta\beta_0^{(p)}) = \exp \left\{ -i\delta\beta_0^{(p)} z \right\} A(z, T, 0). \quad (21)$$

Consequently, $A(z, T, \delta\beta_0^{(p)})$ is periodic in $\delta\beta_0^{(p)}$ with period $\frac{2\pi}{z}$

$$A(z, T, \delta\beta_0^{(p)}) = A\left(z, T, \delta\beta_0^{(p)} + \frac{2\pi}{z}l\right), \quad (22)$$

where l is integer.

3.5 Nonlinear case: self-phase and cross-phase modulations

We examine whether the same periodicity is valid for nonlinear cases and consider NLSE with $\delta\beta_0^{(p)}$ A term

$$i\frac{\partial A}{\partial z} = \frac{\beta_2}{2} \frac{\partial^2 A}{\partial T^2} + \delta\beta_0^{(p)} A + \gamma_S |A|^2 A. \quad (23)$$

In addition, we focus on

$$i\frac{\partial \bar{A}}{\partial z} = \frac{\beta_2}{2} \frac{\partial^2 \bar{A}}{\partial T^2} + \gamma_S |\bar{A}|^2 \bar{A}. \quad (24)$$

Similar to the previous subsection, if we show that

$$A(z, T) = \bar{A}(z, T) \exp \left\{ -i\delta\beta_0^{(p)} z \right\}, \quad (25)$$

then the periodicity with respect to β_0 is proven automatically. Substitution of Eq. (25) into Eq. (23) yields

$$\begin{aligned} & i\frac{\partial \bar{A}}{\partial z} \exp \left\{ -i\delta\beta_0^{(p)} z \right\} + \delta\beta_0^{(p)} \bar{A} \exp \left\{ -i\delta\beta_0^{(p)} z \right\} \\ &= \frac{\beta_2}{2} \frac{\partial^2 \bar{A}}{\partial T^2} \exp \left\{ -i\delta\beta_0^{(p)} z \right\} + \delta\beta_0^{(p)} \bar{A} \exp \left\{ -i\delta\beta_0^{(p)} z \right\} \\ &+ \gamma_S |\bar{A}|^2 \bar{A} \exp \left\{ -i\delta\beta_0^{(p)} z \right\}. \end{aligned}$$

By canceling $\exp \left\{ -i\delta\beta_0^{(p)} z \right\}$ and taking into account Eq. (24) we obtain an identity. Thus, the periodicity property (22) also hold for Eq. (23). Note, in the case of self-phase modulation, the equations for the modes do not depend on each other and can be solved by a PINN independently.

Finally, we consider NLSE for $A \equiv A_p$ with the $\delta\beta_0^{(p)}$ A term and the term $\gamma_C |A_n|^2 A$, $n \neq p$, which governs the cross-phase modulation

$$i\frac{\partial A}{\partial z} = \frac{\beta_2}{2} \frac{\partial^2 A}{\partial T^2} + \delta\beta_0^{(p)} A + \gamma_C |A_n|^2 A. \quad (26)$$

It is worth mentioning that the periodic property of A_n (see Eq. (22)) does not affect A in Eq. (26), whereas the rest of the proof is analogous to that of the self-phase modulation case. Therefore, Eq. (22) is valid for cross-phase modulation as well.

Table 3: Reference and scaled values of $\delta\beta_0^{(p)}$

p	$\delta\beta_0^{(p)}, m^{-1}$	$\widehat{\delta\beta_0^{(p)}}, m^{-1}$	$\left\lfloor \delta\beta_0^{(p)} z / (2\pi) \right\rfloor^*$	L, m
1	0	—	—	—
2	-5662.25183	-0.09655 -1.10186	90116 4505	100 5
3	-11328.0841	-0.0036 -0.7576	180292 9014	100 5

* Integer number of periods

3.6 Scale transformation

Recalling the property (22), we conclude that the solution at the coordinate z does not change if we replace $\delta\beta_0^{(p)}$ with

$$\widehat{\delta\beta_0^{(p)}} = \delta\beta_0^{(p)} + \frac{2\pi}{z}l. \quad (27)$$

Since our goal is to reduce the absolute value of the coefficient by the $\delta\beta_0^{(p)}$ A term we can set

$$\widehat{\delta\beta_0^{(p)}} = \delta\beta_0^{(p)} + \frac{2\pi}{z}l', \quad (28)$$

where

$$l' = \left\lfloor \frac{\delta\beta_0^{(p)} z}{2\pi} \right\rfloor, \quad (29)$$

and the brackets ' $\lfloor \cdot \rfloor$ ' stand for the integer part. According to Eq. (21), for a point x inside the fiber ($0 < x < z$) holds

$$\begin{aligned} & A\left(x, T, \delta\beta_0^{(p)} + \frac{2\pi}{z}l\right) \\ &= \exp\left\{-i\left(\delta\beta_0^{(p)}x + \frac{2\pi}{z}lx\right)\right\} A(x, T, 0). \end{aligned} \quad (30)$$

Thus, the scale transformation (28) for the $\delta\beta_0^{(p)}$ A term affects neither the absolute value of A_p across the entire fiber nor its phase expressed via $\text{Re}A_p$ and $\text{Im}A_p$ at points x , such that lx/z is integer. With help of this scale transformation, we can level the order of the MMNLSE coefficients, thus overcoming the obstacle that prevents PINN from convergence. The reference $\delta\beta_0^{(p)}$ and scaled values $\widehat{\delta\beta_0^{(p)}}$ for different lengths of fiber are summarized in Table 3. As a result of application of the scaled values $\widehat{\delta\beta_0^{(p)}}$, PINN converges, as evidenced by the decreasing loss function. Comparison of loss functions for the original and the scaled values is presented in Fig. 3. Despite the fact, that the absolute value of A does not depend on $\delta\beta_0^{(p)}$, PINN converges neither for real and imaginary parts of A , nor the absolute value of A . We can see that in the case of unscaled dispersion, the loss function starts with very large values and sharply reaches a plateau about values $\sim 10^4$. If the dispersion coefficients are scaled, the loss function starts from $\sim 10^4$ and continues to decrease throughout the training period.

Alternatively, recalling Eq. (21) we have

$$\begin{aligned} A\left(z, T, \delta\beta_0^{(p)}\right) &= \left(\cos\left\{-\delta\beta_0^{(p)}z\right\} + i\sin\left\{-\delta\beta_0^{(p)}z\right\}\right) \\ &\quad \times (\text{Re}A(z, T, 0) + i\text{Im}A(z, T, 0)), \end{aligned} \quad (31)$$

which yields

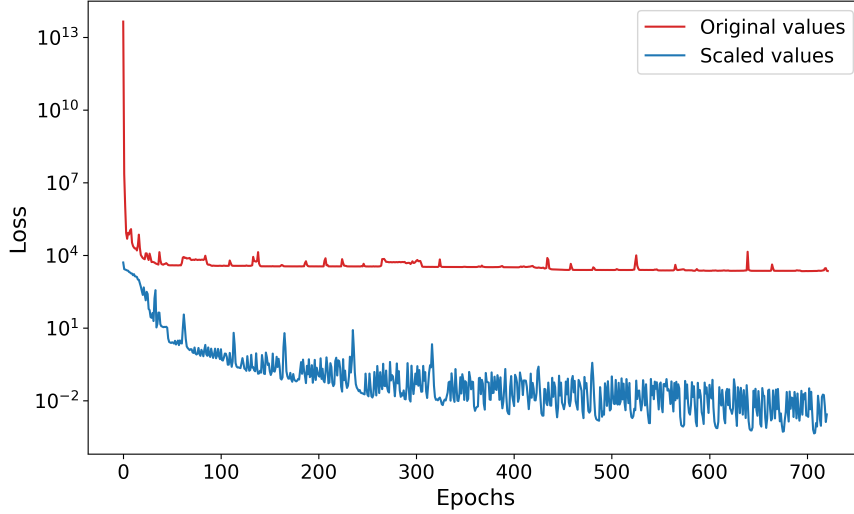


Figure 3: Comparison of the loss functions for the original and scaled values of $\delta\beta_0^{(p)}$

$$\begin{aligned} \text{Re}A(z, T, \delta\beta_0^{(p)}) &= \text{Re}A(z, T, 0) \cos\{-\delta\beta_0^{(p)}z\} \\ &\quad - \text{Im}A(z, T, 0) \sin\{-\delta\beta_0^{(p)}z\}, \end{aligned} \quad (32)$$

$$\begin{aligned} \text{Im}A(z, T, \delta\beta_0^{(p)}) &= \text{Re}A(z, T, 0) \sin\{-\delta\beta_0^{(p)}z\} \\ &\quad + \text{Im}A(z, T, 0) \cos\{-\delta\beta_0^{(p)}z\}. \end{aligned} \quad (33)$$

Thus, PINNs can be applied to Eq. (1) with $\delta\beta_0^{(p)} = 0$ to compute $A(z, T, 0)$. Afterwards, the true values of $\text{Re}A(z, T, \delta\beta_0^{(p)})$ and $\text{Im}A(z, T, \delta\beta_0^{(p)})$ can be restored through Eqs. (32)-(33).

4 Numerical results

We start our numerical analysis with the linear case, since it allows us to determine the upper boundary of the propagation length which can be processed by PINN. In fact, the complexity of the problem increases with the propagation length. Indeed, as z becomes larger than the characteristic lengths L_D and L_{NL} , the effects of dispersion and nonlinearities in fibers become more pronounced resulting high frequency oscillations of $\text{Re}A$ and $\text{Im}A$. According to the F-principle [32], such cases require longer time for training. Consequently, in the linear case, the maximum propagation length is distributed an order of L_D . In the nonlinear case, the maximum propagation length be at most of an order of L_D or shorter depending on the L_{NL} .

We consider linear and nonlinear cases for pulse energies $E = 10$ nJ and $E = 0.1$ nJ. The energy is equally divided between all modes. We choose the energy $E = 10$ nJ because of the small nonlinear length L_{NL} , so we can observe nonlinear effects at small lengths of fibers. On the other hand, the energy $E = 0.1$ nJ is closer to realistic values of energy, so we also consider this energy. The wavelength for all cases is $\lambda = 1030$ nm. The time window is 100 ps. Training time is 2 hours unless otherwise specified. Table 4 presents the dispersion coefficients for different lengths of fiber. The values of $\widehat{\delta\beta_0^{(p)}}$ are computed using the scaling transformation (28)-(29).

We examine the efficiency of scale transformation for a fiber of $L = 100$ m length neglecting nonlinear effects (case 1). The SSF solution for the problem with original values of $\delta\beta_0^{(p)}$ and PINN results with the scaled values of $\delta\beta_0^{(p)}$ are

Table 4: Parameters of fiber and signal

N_e	L , m	p	$\delta\beta_0^{(p)}$, m^{-1}	$\delta\beta_1^{(p)}$, ps/m	$\beta_2^{(p)}/2$, ps^2/m
1	100 / 300	1	0	0	0.01916410
		2	-0.09655858	0.00295601	0.01916082
		3	-0.00364598	0.00791849	0.01915536
2	5	1	0	0	0.01916410
		2	-1.10186823	0.00295601	0.01916082
		3	-0.75762821	0.00791849	0.01915536

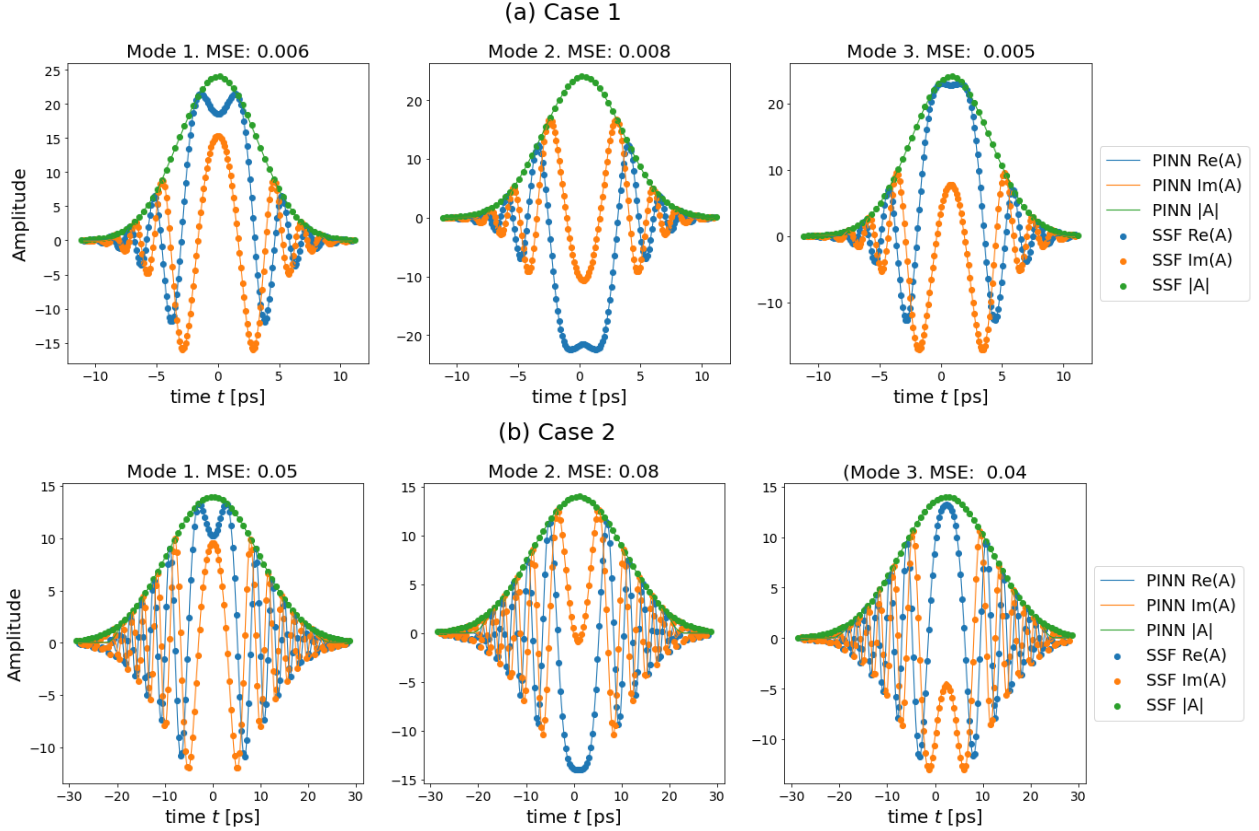


Figure 4: Case 1: three-mode linear case, $E = 10$ nJ, $L = 100$ m. Case 2: three-mode linear case, $E = 10$ nJ, $L = 300$ m.

shown in Fig. 4(a). We see that the scaling of $\delta\beta_0^{(p)}$ allows to reproduce by PINN not only the absolute value of U , but also its real and imaginary parts. Next, we increase the length of the fiber up to $L = 300$ m (case 2) and training time up to 2.5 hours. The results are shown in Fig. 4(b). The training for 300 m requires slightly more time than for 100 m as the solution for 300 m case has much stronger oscillatory behavior (although the increase of the training time is not significant). The agreement between PINN and SSF is obtained keeping the MSE below 0.08.

Now we consider nonlinear cases. The results for the self-phase modulation (case 3) with scaled values of $\beta_0^{(p)}$ are shown in Fig. 5(a). In this example, the fiber length is set to $L = 5$ m, the pulse energy $E = 10$ nJ. One can see that scale transformation provides robust PINN solution in the nonlinear case. Note that for such high values of pulse energy, the nonlinear length L_{NL} is two orders of magnitude less than the dispersion length L_D and the former limits the maximum value of the propagation length solvable by PINN. From Eq. (8) we conclude that in the nonlinear case the maximum fiber length which PINN can handle decreases when the pulse energy increases.

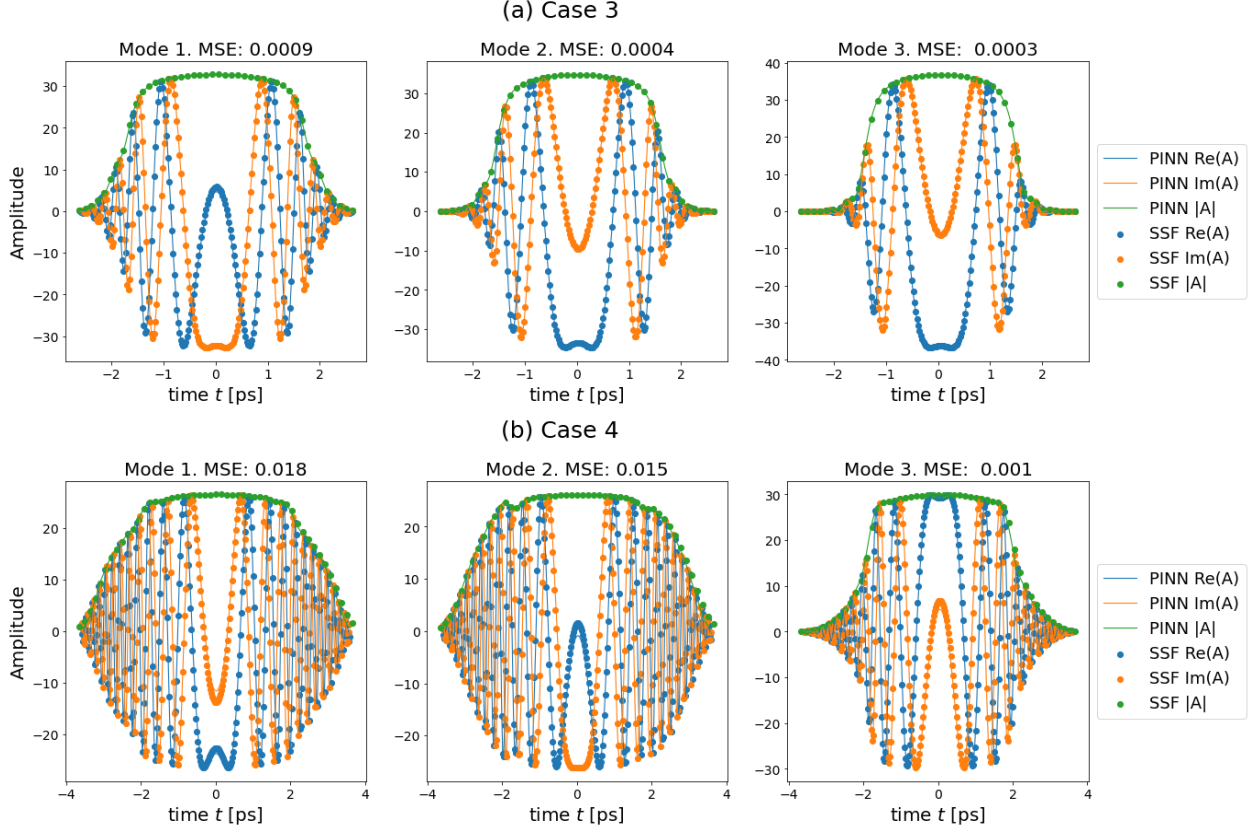


Figure 5: Case 3: three-mode nonlinear case with self-phase modulation, $E = 10$ nJ, $L = 5$ m. Case 4: three-mode nonlinear case with self- and cross-phase modulations, $E = 10$ nJ, $L = 5$ m.

Since in the pure self-phase modulation case (i.e. $\gamma_C^{(n)} = 0$), the equations for three modes are independent, we consider two configurations of PINN. In the first one, a single PINN with six outputs is used to compute three modes (as shown in Fig. 1). In the second configuration, three independent PINNs with two outputs each are used for each mode. Our tests show that the first configuration is just as efficient as the second one. Thus, the number of modes does not impose principal difficulties for PINN.

Finally, we consider examples with both self-phase and cross-phase modulation terms. The results for $E = 10$ nJ and $L = 5$ m (case 4) are illustrated in Fig. 5(b). The equations for three modes are coupled and PINN with six outputs is used to solve a complete system of equations. The scaling procedure of $\delta\beta_0^{(p)}$ provides robust results. Note, that for this case the PINN training requires an increase in training time up to 5 hours due to high frequency oscillations in real and imaginary parts of the solution. Essentially, at high energy $E = 10$ nJ, the nonlinear length L_{NL} becomes several orders of magnitude smaller than the dispersion length L_D , i.e. $L_{NL} \ll L_D$. Thus, at a distance of 5 m, we can clearly observe nonlinear effects. The MMNLSE solution for longer fibers by PINN is a difficult problem and requires substantial increase in the training time.

For pulse energy $E = 0.1$ nJ (which is more realistic in applications), the maximum lengths of fibers which PINN can handle increases. Fig. 6 shows solutions for three-mode nonlinear cases with self- and cross-phase modulations for $E = 0.1$ nJ, $L = 100$ m (Fig. 6(a)) and $L = 300$ m (Fig. 6(b)) (that are case 5 and case 6, respectively). We can see that the default configuration of PINN with 240000 sampling points (see Section 2) yields good accuracy for case 5. By increasing the length of the fiber up to 300 m, the number of points has to be increased up to 880000 dots and the training time up to 4 hours. Note that the increased fiber length combined with nonlinear effects causes high-frequency oscillations at the edges of the real and imaginary parts of the pulse, which PINN cannot handle according to the F-principle. The results show that the maximum length of fibers PINN can handle depends on L_D and L_{NL} . We found empirically that this length is about $\min(50L_D, 50L_{NL})$.

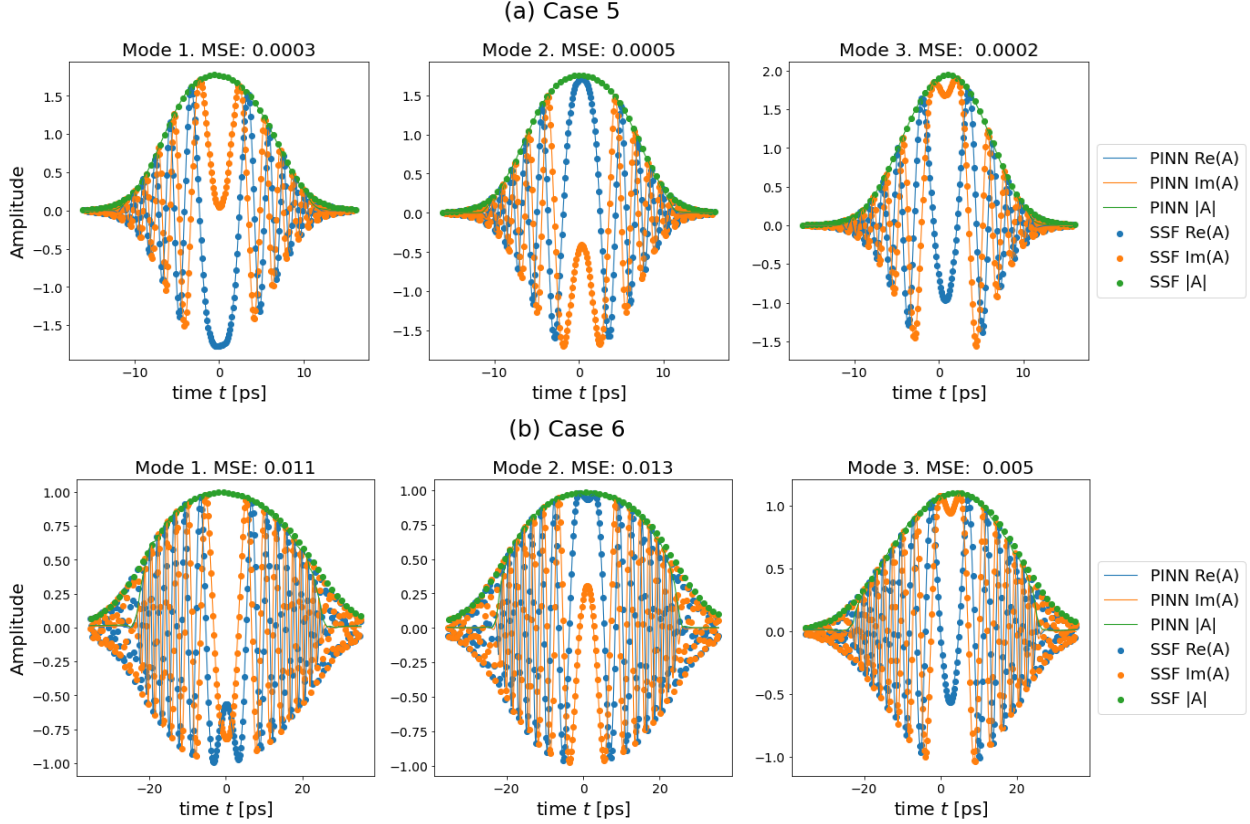


Figure 6: Case 5: three-mode nonlinear case with self- and cross-phase modulations, $E = 0.1$ nJ, $L = 100$ m. Case 6: three-mode nonlinear case with self- and cross-phase modulations, $E = 0.1$ nJ, $L = 300$ m.

5 Conclusion

In this paper, the PINN has been applied to solve the MMNLSE. It was shown that the zeroth order dispersion term in the MMNLSE causes high frequency oscillations which add severe complexity for PINN. Even if the absolute value of the temporal envelope goes not depend on $\delta\beta_0^{(p)}$, PINN is not able to reproduce neither real and imagery parts of the electric field temporal envelope, nor its absolute value. It was shown that two factors impose computational difficulty for PINN. The first one is the large difference of coefficients at terms of MMNLSE. As a matter of fact, the optimizers used during the PINN training might not capture the influence of terms with low coefficients. This problem can be partially solved by using the frame transformation and normalization, which however do not resolve the difficulty associated with the $\delta\beta_0^{(p)}$ -term. The second factor is high oscillations in the solution. In addition, the training time increases significantly according to the F-principle [32, 33], which states that a deep neural network tends to learn a target function from low to high frequencies during the training. Note that the F-principle limitation can be also used to explain why PINNs fail when the fiber length becomes significantly larger than the dispersion and the nonlinear lengths.

In this study a novel scaling transformation to $\delta\beta_0^{(p)}$ for the MMNLSE solution by PINN has been proposed. A good agreement is obtained between PINN and SSF. To our knowledge, it is the first successful application of PINNs to the MMNLSE. Results are obtained for fiber lengths up to 300 m for the pulse energy 10 nJ for linear cases and 300 m for the pulse energy 0.1 nJ for nonlinear cases taking into account self- and cross-phase modulations. We note that including the cross-phase modulation term increases the training time by two times as compared to the self-phase modulation case. Besides, increasing the fiber length may require both an increase in time and a multiple increase in the number of points. The maximum fiber length which PINN can handle depends on the dispersion length L_D and nonlinear length L_{NL} . Empirically we have found that the maximum length can be roughly estimated as

$\min(50L_D, 50L_{NL})$. Note that since L_{NL} depends on the pulse energy (see Eq. (8)), for a given fiber length there is a maximum value of the pulse energy PINN can handle.

In our future work we aim to include four wave mixing and Raman effect in PINN as well as to apply the transfer learning technique [34, 35] which promises drastic computational savings compared to classical approaches once the PINN has been trained. Also, another perspective would be to study the performance of PINN for MMNLSE using a novel network weight initialization scheme called Reptile described in [36].

Appendix: solution for the single mode linear case

Here, we summarize basic steps for solving Eq. (9) following [2]. We consider a linear single mode equation for $A(z, T)$

$$i \frac{\partial A}{\partial z} = \frac{\beta_2}{2} \frac{\partial^2 A}{\partial T^2}. \quad (34)$$

Performing Fourier transform we obtain

$$i \frac{\partial \hat{A}}{\partial z} = -\frac{1}{2} \beta_2 \omega^2 \hat{A}. \quad (35)$$

Eq. (35) can be analytically integrated

$$\hat{A}(z, \omega) = \hat{A}(0, \omega) \exp \left\{ \frac{i}{2} \beta_2 \omega^2 z \right\}. \quad (36)$$

The inverse Fourier transform reads as

$$A(z, T) = \frac{1}{2\pi} \int_{-\infty}^{+\infty} \hat{A}(0, \omega) \times \exp \left\{ \frac{i}{2} \beta_2 \omega^2 z - i\omega T \right\} d\omega, \quad (37)$$

where

$$\hat{A}(0, \omega) = \frac{1}{2\pi} \int_{-\infty}^{+\infty} U(0, T) \exp \{ \omega T \} dT. \quad (38)$$

As the initial condition, we consider a Gaussian pulse given by

$$A(0, T) = \exp \left\{ -\frac{T^2}{2T_0^2} \right\}, \quad (39)$$

where T_0 is a half-width. Then applying Fourier transform to Eq. (39), we obtain

$$\hat{A}(0, \omega) = T_0 \exp \left\{ -\frac{1}{2} T_0^2 \omega^2 \right\}. \quad (40)$$

Substituting Eq. (40) into Eq. (37) yields

$$A(z, T) = \frac{1}{2\pi} \int_{-\infty}^{+\infty} T_0 \exp \left\{ -\frac{1}{2} T_0^2 \omega^2 \right\} \times \exp \left\{ \frac{i}{2} \beta_2 \omega^2 z - i\omega T \right\} d\omega. \quad (41)$$

Setting $a = \left(\frac{i}{2} \beta_2 z - \frac{1}{2} T_0^2 \right)$ and $b = iT$ and using the following expression

$$\int_{-\infty}^{+\infty} \exp(a\omega^2 + b\omega) d\omega = \sqrt{\frac{\pi}{-a}} \exp\left(-\frac{b^2}{4a}\right), \quad (42)$$

we find that

$$A(z, T) = \frac{T_0}{2\pi} \sqrt{\frac{\pi}{-\left(\frac{i}{2}\beta_2 z - \frac{1}{2}T_0^2\right)}} \times \exp\left[-\frac{(iT)^2}{4\left(\frac{i}{2}\beta_2 z - \frac{1}{2}T_0^2\right)}\right], \quad (43)$$

and after rearranging, we obtain Eq. (12).

References

- [1] P. J. Winzer, Scaling optical fiber networks: Challenges and solutions, *Opt. Photon. News* 26 (3) (2015) 28–35. doi:10.1364/OPN.26.3.000028. URL <http://www.optica-opn.org/abstract.cfm?URI=opn-26-3-28>
- [2] G. P. Agrawal, *Fiber-Optic Communication Systems*, Wiley, 2021. doi:10.1002/9781119737391.
- [3] B. J. Puttnam, G. Rademacher, R. S. Luís, Space-division multiplexing for optical fiber communications, *Optica* 8 (9) (2021) 1186–1203. doi:10.1364/OPTICA.427631.
- [4] G. Rademacher, B. J. Puttnam, R. S. Luís, T. A. Eriksson, N. K. Fontaine, M. Mazur, H. Chen, R. Ryf, D. T. Neilson, P. Sillard, F. Achten, Y. Awaji, H. Furukawa, Peta-bit-per-second optical communications system using a standard cladding diameter 15-mode fiber, *Nature Communications* 12 (1) (2021) 4238. doi:10.1038/s41467-021-24409-w.
- [5] O. V. Sinkin, R. Holzlohner, J. Zweck, C. R. Menyuk, Optimization of the split-step fourier method in modeling optical-fiber communications systems, *J. Lightwave Technol.* 21 (1) (2003) 61–68. doi:10.1109/JLT.2003.808628.
- [6] J. Shao, X. Liang, S. Kumar, Comparison of split-step fourier schemes for simulating fiber optic communication systems, *IEEE Photonics J.* 6 (4) (2014) 1–15. doi:10.1109/JPHOT.2014.2340993.
- [7] S. Addanki, I. Amiri, P. Yupapin, Review of optical fibers-introduction and applications in fiber lasers, *Results in Physics* 10 (2018) 743–750. doi:https://doi.org/10.1016/j.rinp.2018.07.028.
- [8] Z. Li, D. Guo, R. Gao, Coded modulation and impairment compensation techniques in optical fiber communication, in: G. Huerta-Cuellar (Ed.), *Fiber Optics*, IntechOpen, Rijeka, 2021, Ch. 4. doi:10.5772/intechopen.98811.
- [9] X. Jiang, D. Wang, Q. Fan, M. Zhang, C. Lu, A. P. T. Lau, Physics-informed neural network for nonlinear dynamics in fiber optics, *Laser Photon. Rev.* 16 (9) (2022) 2100483. doi:10.1002/lpor.202100483.
- [10] M. Raissi, P. Perdikaris, G. E. Karniadakis, Physics informed deep learning (part i): Data-driven solutions of nonlinear partial differential equations, *arXiv preprint arXiv:1711.10561* (2017).
- [11] S. Markidis, The old and the new: Can physics-informed deep-learning replace traditional linear solvers?, *Frontiers in Big Data* 4 (2021). doi:10.3389/fdata.2021.669097.
- [12] C. T. Kelley, *Iterative methods for linear and nonlinear equations*, Society for Industrial and Applied Mathematics, 1995.
- [13] J. Reddy, *Introduction to the finite element method 4E*, 4th Edition, McGraw-Hill Education, Columbus, OH, 2018.

- [14] Weinan, B. Yu, The deep Ritz method: A deep learning-based numerical algorithm for solving variational problems, *Commun. Math. Stat.* 6 (1) (2018) 1–12. doi:10.1007/s40304-018-0127-z.
- [15] C. Monterola, C. Saloma, Solving the nonlinear Schrodinger equation with an unsupervised neural network, *Opt. Express* 9 (2) (2001) 72–84.
- [16] C. Monterola, C. Saloma, Solving the nonlinear Schrödinger equation with an unsupervised neural network: estimation of error in solution, *Optics Communications* 222 (1-6) (2003) 331–339. doi:10.1016/s0030-4018(03)01570-0.
- [17] X. Jiang, D. Wang, Q. Fan, M. Zhang, C. Lu, A. P. Tao Lau, Solving the nonlinear Schrödinger equation in optical fibers using physics-informed neural network, in: *2021 Optical Fiber Communications Conference and Exhibition (OFC)*, 2021, pp. 1–3.
- [18] M. Raissi, P. Perdikaris, G. E. Karniadakis, Physics-informed neural networks: A deep learning framework for solving forward and inverse problems involving nonlinear partial differential equations, *Journal of Computational Physics* 378 (2019) 686–707. doi:10.1016/j.jcp.2018.10.045.
- [19] Y. Shin, On the convergence of physics informed neural networks for linear second-order elliptic and parabolic type PDEs, *Communications in Computational Physics* 28 (5) (2020) 2042–2074. doi:10.4208/cicp.oa-2020-0193.
- [20] A. D. Jagtap, G. E. Karniadakis, Extended physics-informed neural networks (XPINNs): A generalized space-time domain decomposition based deep learning framework for nonlinear partial differential equations, *Communications in Computational Physics* 28 (5) (2020) 2002–2041. doi:10.4208/cicp.oa-2020-0164.
- [21] A. D. Jagtap, E. Kharazmi, G. E. Karniadakis, Conservative physics-informed neural networks on discrete domains for conservation laws: Applications to forward and inverse problems, *Computer Methods in Applied Mechanics and Engineering* 365 (2020) 113028. doi:10.1016/j.cma.2020.113028.
- [22] J. Yu, L. Lu, X. Meng, G. E. Karniadakis, Gradient-enhanced physics-informed neural networks for forward and inverse PDE problems, *Computer Methods in Applied Mechanics and Engineering* 393 (2022) 114823. doi:10.1016/j.cma.2022.114823.
- [23] L. Sun, H. Gao, S. Pan, J.-X. Wang, Surrogate modeling for fluid flows based on physics-constrained deep learning without simulation data, *Comput. Methods Appl. Mech. Eng.* 361 (112732) (2020) 112732.
- [24] F. Sahli Costabal, Y. Yang, P. Perdikaris, D. E. Hurtado, E. Kuhl, Physics-informed neural networks for cardiac activation mapping, *Front. Phys.* 8 (Feb. 2020). doi:10.3389/fphy.2020.00042.
- [25] D. Zhang, L. Guo, G. E. Karniadakis, Learning in modal space: Solving time-dependent stochastic PDEs using physics-informed neural networks, *SIAM J. Sci. Comput.* 42 (2) (2020) A639–A665. doi:10.1137/19M1260141.
- [26] S. Cuomo, V. S. Di Cola, F. Giampaolo, G. Rozza, M. Raissi, F. Piccialli, Scientific machine learning through Physics-Informed neural networks: Where we are and what’s next, *J. Sci. Comput.* 92 (3) (Sep. 2022). doi:10.1007/s10915-022-01939-z.
- [27] S. Wang, X. Yu, P. Perdikaris, When and why PINNs fail to train: A neural tangent kernel perspective, *Journal of Computational Physics* 449 (2021) 110768. doi:10.1016/j.jcp.2021.110768.
- [28] S. Wang, H. Wang, P. Perdikaris, On the eigenvector bias of fourier feature networks: From regression to solving multi-scale PDEs with physics-informed neural networks, *Computer Methods in Applied Mechanics and Engineering* 384 (2021) 113938. doi:10.1016/j.cma.2021.113938.
- [29] A. Paszke, S. Gross, F. Massa, A. Lerer, J. Bradbury, G. Chanan, T. Killeen, Z. Lin, N. Gimelshein, L. Antiga, A. Desmaison, A. Kopf, E. Yang, Z. DeVito, M. Raison, A. Tejani, S. Chilamkurthy, B. Steiner, L. Fang, J. Bai, S. Chintala, Pytorch: An imperative style, high-performance deep learning library, in: *Advances in Neural Information Processing Systems* 32, Curran Associates, Inc., 2019, pp. 8024–8035. URL <http://papers.nips.cc/paper/9015-pytorch-an-imperative-style-high-performance-deep-learning.pdf>

-
- [30] X. Glorot, Y. Bengio, Understanding the difficulty of training deep feedforward neural networks, in: Y. W. Teh, M. Titterton (Eds.), Proceedings of the Thirteenth International Conference on Artificial Intelligence and Statistics, Vol. 9 of Proceedings of Machine Learning Research, PMLR, Chia Laguna Resort, Sardinia, Italy, 2010, pp. 249–256.
URL <https://proceedings.mlr.press/v9/glorot10a.html>
- [31] Y. Zang, Z. Yu, K. Xu, M. Chen, S. Yang, H. Chen, Universal fiber models based on PINN neural network, in: Asia Communications and Photonics Conference 2020, no. M4A.266, OSA, 2020.
URL <https://ieeexplore.ieee.org/document/9365071>
- [32] Z.-Q. J. Xu, Frequency principle in deep learning with general loss functions and its potential application (2018). doi:10.48550/ARXIV.1811.10146.
- [33] D. A. Roberts, S. Yaida, B. Hanin, The Principles of Deep Learning Theory: An Effective Theory Approach to Understanding Neural Networks, Cambridge University Press, 2022. doi:10.1017/9781009023405.
- [34] S. Goswami, C. Anitescu, S. Chakraborty, T. Rabczuk, Transfer learning enhanced physics informed neural network for phase-field modeling of fracture, Theor. Appl. Fract. Mech. 106 (102447) (2020) 102447. doi:10.1016/j.tafmec.2019.102447.
- [35] X. Chen, C. Gong, Q. Wan, L. Deng, Y. Wan, Y. Liu, B. Chen, J. Liu, Transfer learning for deep neural network-based partial differential equations solving, Adv. Aerodyn. 3 (1) (Dec. 2021). doi:10.1186/s42774-021-00094-7.
- [36] X. Liu, X. Zhang, W. Peng, W. Zhou, W. Yao, A novel meta-learning initialization method for physics-informed neural networks, Neural Comput. Appl. (May 2022). doi:10.1007/s00521-022-07294-2.